1

2

3

4

5

6

7

8

9

10

11

12 **The long-wave infrared (8-12 μm) spectral features of selected rare earth element –**
13 **bearing carbonate, phosphate and silicate minerals**

14

15

16

17 Kati Laakso[a*], David J. Turner[b], Benoit Rivard[a] and Arturo Sánchez-Azofeifa[a]

18

19
20 [a] Centre for Earth Observation Sciences (CEOS), Department of Earth and Atmospheric
21 Sciences, University of Alberta, Edmonton, Alberta T6G 2E3, Canada
22 [b] Department of Earth, Ocean and Atmospheric Sciences, University of British Columbia,
23 Vancouver, British Columbia V6T 1Z4, Canada
24 * The corresponding author, corresponding author email: laakso@ualberta.ca

25

26

27 November 12, 2018

28

29

30

31

Abstract

Rare earth elements (REEs) are a group of metals essential to high technology industries. This high demand, combined with a high supply risk, has led to an understanding that REEs are critical to society. Despite the potential that hyperspectral imaging (HSI) data offers for a fast and non-invasive characterization of the REEs, it is still poorly understood whether REEs have some information in the long-wave infrared (LWIR; 8-12 μm) wavelength range that can be used for their identification. To partially fill this gap, we have investigated the spectroscopy of twelve REE-bearing mineral samples using relatively high spatial and spectral resolution LWIR hyperspectral imaging data. These samples were formerly characterized using electron probe microanalysis (EPMA), scanning electron microscopy (SEM), and hyperspectral imaging data acquired in the 0.4-2.5 μm wavelength range. Results from these analyses were compared to and used to guide the analysis of the HSI data recorded in the LWIR range. This information was further compared to a reference spectral library of rare earth oxides. Our findings suggest that the spectral features of the samples can generally be traced to the asymmetric degenerate stretching and bending modes of the X-O (X = C, Si, P) groups. Moreover and contrary to what has been observed in the shorter wavelengths, there are no definitive spectral features in the LWIR wavelength region that could be assigned to any specific REE.

1. Introduction

Rare earth elements (REEs) are a group of 17 chemically similar elements that cover fifteen lanthanides (atomic numbers 57-71 in the periodic table), plus scandium and yttrium (atomic numbers 21 and 39, respectively). In 2017, China held circa 81% of the global production of REEs (U.S. Geological Survey, 2018), a geopolitical supply risk that has, in combination with the extensive use of REEs for several high technology applications, contributed to the European Commission (2017) and the U.S. Department of Energy (2011) in classifying REEs as "critical". In addition to their uneven global distribution, the availability of the REEs is determined by their natural abundance variation that favors elements with lower, rather than higher atomic numbers, and those with even, rather than odd, atomic numbers, factors that may not always align with the actual demand of specific REEs. These factors conspire to create an imbalance between supply and demand, a problem that can be mitigated through complex technical solutions and political interventions (Binnemans and Jones, 2015).

The recognition of the importance of REEs has led to a range of research exploring the possibilities of applying hyperspectral technology to their detection. These investigations have mainly focused on the visible to near-infrared (VNIR; 0.4-1.3 μm) and short-wave infrared (SWIR; 1.3-3.0 μm) wavelength regions where the REEs display a series of well-defined, sharp absorption features induced by electronic processes (VNIR wavelength range) and REE-OH vibrational overtones (SWIR wavelength range; Dieke, 1968; Hunt et al., 1972; Rowan et al., 1986 and references therein). More recent investigations in the SWIR region (Turner et al., 2014; 2016; 2018) have provided a wealth of spectral information relevant to the hyperspectral identification and detection of REE-bearing minerals. Despite clear absorptions that cannot be confused with that of other VNIR-active minerals, the presence of iron oxides, active in the same wavelength range, can hamper the detection of the REEs even in small quantities (Boesche et al., 2015). Moreover, the spectral features of different REEs overlap both in the VNIR and SWIR wavelength regions (e.g. Turner et al., 2014, 2016, 2018), making it challenging to identify with certainty the presence of a specific rare earth element in a mineral in many cases.

Fewer studies have applied hyperspectral technology to the detection of the REEs in the long-wave infrared wavelength range (LWIR; 8-12 μm). In this wavelength range, the spectral features of minerals are induced by a combination of Restrahlen, Christiansen and transparency features (Salisbury et al. 1987). The most prominent of these features, and the

85   focus of this study, are the Restrahlen features that result from the fundamental molecular
86   vibrations of minerals, and that are expressed as reflectance maxima in the mineral
87   spectrum. These maxima arise from the high absorption coefficients of minerals that results
88   in a mirror like effect and thus in high reflectance values (e.g., Salisbury et al. 1987).
89   One of the first investigations extending into the LWIR wavelength range was
90   conducted by Dieke (1968). The author documented the locations of the many $4f$-$4f$
91   electronic transitions ("Dieke diagram" from herein), including a suite of base energy levels
92   in the LWIR and in particular for Ce^{3+} that does not exhibit diagnostic absorptions in the
93   VNIR or SWIR. Another early work by Adler and Kerr (1963) reported spectral features of
94   several REE-bearing carbonate minerals, but did not specifically discuss the potential effect
95   of the REEs in mineral spectra. This also applies to a range of studies that applied
96   hyperspectral data to study REE-bearing minerals (e.g. Farmer, 1974; Ross 1974; White,
97   1974; Frost and Dickfos, 2007; Frost et al., 2013). A more recent study by Neave et al.
98   (2016) used LWIR hyperspectral data to the investigate a range of REE-bearing rocks,
99   predominantly carbonatitic. While the authors discussed the spectral features of several
100 minerals in the LWIR, references to the impacts of the REEs on the mineral spectra were
101 limited to a potential Sm feature near 10 μm in one of the samples. Spectral databases, such
102 as the RRUFF (Lafuente et al., 2015), the USGS spectral library (Kokaly et al., 2017) and a
103 publication by Chukanov (2014) comprise many examples of REE-bearing minerals, but
104 contain limited information as to the origins of the spectral features in minerals.
105   Prior investigations have provided a solid knowledge base relevant to the
106 hyperspectral identification and detection of REE-bearing minerals, information that can be
107 exploited for the exploration of REEs at a variety of spatial scales. Essentially absent
108 however is equivalent information in the LWIR, leaving open the possibility that unique or
109 complementary information applicable for the identification of REE-bearing minerals resides
110 in this range. The question is relevant given the increased availability of remote sensing
111 capabilities in the LWIR due to the emergence of new hyperspectral imaging (HSI)
112 instruments (Feng et al., 2018).
113   In this context, and with the goal of contributing to partially fill the knowledge gap of
114 the influence of the REEs in the LWIR wavelength range, we investigated a set of samples
115 that encompass seven REE-bearing minerals. Using these samples, we discuss the likely
116 provenance of spectral features, and the implications that these features have on the
117 identification of REEs by HSI spectroscopy. This technology not only allows for the
118 mineralogy of the samples to be identified, but also makes possible the determination of the
119 spatial distribution of their mineralogy.
120
121 **2. Materials and data acquisition**

122 *2.1 Sample suite*

123
124   Twelve REE-bearing mineral samples were chosen to represent the fluorocarbonates
125 (one bastnasite and one parisite sample), phosphates (one monazite and three xenotime
126 samples) and silicates (three eudialyte samples, one mosandrite sample and two zircon
127 samples). All the samples were obtained from private collections of A. Mariano and D.
128 Turner. The samples, their dimensions and localities are listed in Table 1.
129   Samples 1-6 are monomineralic as opposed to samples 7-9 that are either single
130 crystals or coarse polycrystalline aggregates of more than one mineral. Samples 10-12
131 comprise two or more minerals that either occur as irregular clusters of an average diameter
132 of 7.5 to 25 mm (samples 10-11) or as isolated crystals of up to 8 mm in diameter (sample
133 12). The dimensions of the samples and their mineral occurrences are given in Table 1.

134 *2.2 Electron probe microanalyzer data acquisition*

135

136 The Philips XL30 scanning electron microscope (SEM) at the University of British
137 Columbia was first used to investigate the potential chemical zoning of the samples and
138 ensure chemical homogeneity. Mineral chemistry was then determined using electron probe
139 microanalyzer (EPMA) facilities of the Saskatchewan Research Council's Advanced
140 Microanalysis Centre. The analyses were conducted using a Cameca SX-100 equipped with
141 5 tunable, wavelength dispersive spectrometers, using a 40° takeoff angle, beam energy of
142 15 keV, beam current of 20 nA and beam diameter of 5 μm. The results from these analyses
143 show that the samples are unzoned and the sample suite shows variable quantities of the
144 lanthanides (see Table 2 for details).

2.3 Hyperspectral data acquisition and preprocessing

147 To investigate the spectral features of the samples in the LWIR wavelength range,
148 hyperspectral laboratory data were acquired using the AisaOWL spectrometer (Harris et al.,
149 2017) mounted on a SisuROCK imaging system by Specim (Spectral Imaging Ltd., Oulu,
150 Finland). These LWIR data were acquired in the 7.279-20.797 μm wavelength range with a
151 47 nm sampling interval, 100 nm spectral resolution (bandwidth) and 0.7 mm spatial
152 resolution.
153 The preprocessing of the hyperspectral image took place in two steps. First, the data
154 were spectrally cropped to the 7.797-12.366 μm spectral range (98 bands) to remove bands
155 with a low signal-to-noise ratio and poor instrument responsivity. Second, the raw data
156 acquired were converted to reflectance using the aluminum standard and a blackbody cavity
157 of the imaging frame.

3 Spectral analysis

160 A representative spectrum was acquired from the imagery of each sample by
161 selecting 3 to 4 pixels to represent spectra with the highest available signal-to-noise-ratios
162 and purest representation of the mineral in question. This selection was conducted based on
163 visual observations and expert knowledge on mineral spectroscopy. In the case of the rock
164 samples 10-12, previous knowledge on the spatial distribution of different minerals was used
165 in the selection process. Furthermore, the spectral shapes of mosandrite and zircon,
166 extracted from the rock samples 10-12, were compared against those published by
167 Chukanov (2014). The selected pixels (see Table 1 for an exact number per sample),
168 assessed to be an optimal set to represent the spectral features of the samples, were
169 subsequently averaged to form a representative spectrum for each mineral.
170 After extracting an average spectrum of each sample, the spectra were investigated
171 for features that were subsequently recorded in Table 3 and labeled as *f1-f8*. If it was
172 assessed that a spectral feature was induced by a specific fundamental vibrational process,
173 the same label was used throughout the sample set.
174 Finally, a visual comparison was conducted between the sample spectra and those
175 of pure rare earth oxides, published by Sheibley and Fowler (1966). In this analysis, the REE
176 composition of the samples, acquired through the EPMA analysis, (see section 2.2 for
177 details), was used to compare the features of the samples against those of the REEs known
178 to be present in the sample.

4 Results

4.1 Carbonate minerals

183 The spectral range between 8 and 9 μm has little coherent data in the case of the
184 carbonate mineral samples, and was therefore omitted from further data analysis. The

185 bastnaesite sample presented a subtle spectral feature near 9.2 µm, absent or uncertain in
186 the parisite sample 2 (label *f1*, Fig. 1).
187   All the carbonate mineral samples have a pronounced spectral feature between 11
188 and 12 µm that is at slightly shorter wavelengths in parisite than in bastnasite (label *f2*, Fig.
189 1).

4.2 Phosphate minerals

191
192   The phosphate minerals monazite (sample 3) and xenotime (samples 4-6) have a
193 pronounced spectral feature that is located between 9 and 10 µm. The spectral feature,
194 labeled *f3* and *f4* in Figs. 2a-c, comprises two reflectance maxima. In samples 5 and 6 this
195 feature marks the general reflectance maximum, but in samples 3 and 4 the reflectance
196 again rises toward 12 µm after lower reflectance values near 10.5 µm.
197   Xenotime samples 4-6 also display a spectral feature near 8.6 µm (label *f5*, Figs. 2b-
198 c).

4.3 Silicate minerals

200
201   The silicate minerals investigated include eudialyte in samples 7 to 9, mosandrite in
202 sample 10 and zircon in samples 11 and 12.
203   The eudialyte sample 7 has a spectral feature labeled *f6* near 8.739 µm (Fig. 3). This
204 feature is not present or detectable in the other eudialyte samples (Fig. 3) or in the
205 mosandrite sample (Fig. 4a). We also tentatively assign this label (*f6*) to the spectral feature
206 near 8.833 µm in the zircon sample 11 (Fig. 4b) due to the close proximity of the features
207 (8.739 µm in sample 7 and 8.833 µm in sample 11) in the electromagnetic spectrum.
208   All the silicate samples show a pronounced spectral feature near 9.5-11 µm (Figs. 3
209 and 4a-b). In samples 7 and 9 this reflectance maximum is split into two. The first spectral
210 peak is identified as *f7* and the second peak being is identified as *f8* (Fig. 3). Contrary to this,
211 mosandrite and zircon only have one reflectance maximum labeled as *f8* in Figs. 4a-b.

5. Interpretation of the spectral features

5.1 Carbonate minerals

214
215   The prominent reflectance peak of the carbonate mineral samples 1 and 2, located
216 between 11 and 12 µm (label *f2* in Fig. 1), can be traced to the asymmetric deformational
217 (bending) mode v_2 of the CO_3^{2-} ion (Adler and Kerr, 1963; Salisbury et al., 1987;
218 Gunasekaran et al., 2006). The subtler spectral feature near 9.3 µm (label *f1* in Fig. 1),
219 present in bastnasite (sample 1) has been attributed to the v_1 stretching mode of CO_3^{2-} ion
220 by Adler and Kerr (1963). The appearance of this feature was assigned by Adler and Kerr
221 (1963) and White (1974) to increasing disorder in the CO_3^{-2} ion.

5.2 Phosphate minerals

223
224   The spectral features that occur in the phosphate mineral samples between 9.3 and
225 9.9 µm, labeled as *f3* and *f4* in Figs. 2a-c, have been assigned to the triply degenerate
226 antisymmetric stretching modes v_3 of the PO_4^{-3} tetrahedra (e.g., as in Kravitz et al. 1968,
227 Begun et al. 1981, Christensen et al. 2000 and Heuser et al. 2014). Frost et al. (2015)
228 reported a spectral feature near 8.5 µm, also present in samples 4-5 near 8.6 µm (label *f5* in
229 Figs. 2b-c) and attributed the spectral feature to the PO_4^{-3} v_3 antisymmetric stretching mode
230 in vantasselite ($Al_4(PO_4)_3(OH)_3 \cdot 9H_2O$).

5.3 Silicate minerals

The silicate mineral samples generally display one to three spectral features in the 8-12 µm wavelength range (labels *f6-f8* in Figs. 3 and 4a-b). Spectral features in this range have been assigned to the degenerate, asymmetric stretching vibrations of the v_3 mode of the Si-O-Si tetrahedra (e.g. Salisbury et al.,1991).

Samples 7 and 11 (eudialyte and zircon, respectively) have a spectral feature near 8.7-8.8 µm (label *f6* in Figs. 3 and 4b). A similar spectral feature was reported by Rastsvetaeva et al. (2018) near 9.4 µm and assigned to the Si-O stretching vibrations of tetrahedral rings. Furthermore, Lippincott et al. (1958) assigned a spectral feature in cristobalite near 8.3 µm to the Si-O stretching modes of the mineral. A potential provenance for this spectral feature was given by Zhang et al. (2000) who reported the appearance of a spectral feature between 8.7 and 9.5 µm in zircon and attributed this feature to the v_3 Si-O stretching vibrations induced by radioactive decay. Zircon commonly contains radioactive elements, such as U and Th, that can, as a result of such decay, damage the structure of zircon, resulting in increasing asymmetry and the appearance of new spectral features.

All the silicate samples display an intense spectral feature between 9.5 and 11 µm (labels *f7* and *f8* in Figs. 3 and 4). In the eudialyte samples these features occur between 9.5 and 9.9 µm. Rastsvetaeva et al. (2018) assigned the reflectance maxima between 9.4 and 10.8 µm in eudialyte to the Si-O stretching vibrations of the silica tetrahedra. Contrary to the eudialyte samples 7 and 9, the eudialyte sample 8 and the zircon and mosandrite samples only display one clear reflectance maximum (label *f8* in Figs. 3 and 4a-b) between 9.5-11 µm. Farmer (1974) attributed this spectral feature to the triply degenerate v_3 stretching mode in zircon.

To summarize, we follow the aforementioned investigations and assign the spectral features *f6-f8* of the silicate minerals to the asymmetric v_3 stretching modes of the Si-O-Si tetrahedra.

6. Discussion

The samples of this study were previously well characterized using scanning electron microscopy, electron probe microanalysis and hyperspectral imaging in the VNIR and SWIR wavelength ranges (e.g., Turner, 2015). That body of work documented that all the samples studied here have spectral features in the VNIR and SWIR wavelength ranges associated with the lanthanides. Contrary to what was observed in previous studies focused on the shorter wavelength regions, no spectral features were encountered in the samples that could be unequivocally assigned to REEs and all the reported spectral features of the samples are attributable to the C-O, P-O and Si-O fundamental bending and stretching modes of the carbonate, phosphate and silicate minerals, respectively. This result follows and confirms similar findings by Frost and Dickfos (2007) who observed that even considerable amounts of REEs in bastnasite, parisite and northupite did not change the symmetry of the carbonate anions.

Three phenomena merit discussion in the context of our results: 1) the variable number of spectral features in the samples; 2) the shifting of spectral features; and 3) the state-of-the-art of the current commercially available LWIR imaging spectrometers and their wavelength ranges.

First, the presence of a different number of spectral features (within the same mineral) in the samples (eudialyte, Fig. 3 and zircon, Fig. 4b) can - to some extent - vary depending on the technical qualities of the spectrometer used, and in that regard, first and foremost, their spectral resolution. Also, factors such as spectral mixing can cause spectral features to appear or disappear. Despite the fact that care was taken to isolate the minerals of interest in the rock samples, some spectral mixing is possible especially in the marginal areas where the contents of the pixels are shared by two or more components (e.g. the background material or two to several minerals). Generally, spectral mixing can occur when

the pixel size of an image is larger than the size of individual objects in the pixels (Keshava and Mustard, 2002). As the spatial resolution (0.7 mm) of our hyperspectral image is higher than the size of even the smallest mineral grains in the rock samples (7.5 mm), significant spectral mixing is unlikely to occur. In addition to potential spectral mixing, the observed differences in the number of spectral features can result from structural distortion (lowering of the crystal symmetry) that can be induced by factors such as radiation-induced damage (Zhang and Salje, 2001). As shown by Salisbury et al. (1991), different crystal orientations can also affect the number of spectral features that can be detected in the sample, a factor unlikely to play a role in the rock samples due to their lack of preferred directions of crystal orientation.

Second, wavelength shifting that was observed (within the same mineral) in certain samples (see spectral features *f3, f4, f7 and f8* in Figs. 2, 3 and 4b) has been widely studied in the shorter wavelengths (e.g. Duke, 1994). In the context of the LWIR wavelength range, Begun et al. (1981), Kijkowska at al (2003), Silva et al. (2006) and Heuser et al. (2014) have documented general spectral shifts toward shorter wavelengths in the normal modes of synthetic lanthanide orthophosphates. This shift, that takes place with increasing atomic numbers and respectively, decreasing ionic radii, occurs due to the lanthanide contraction where the crystal radii of the REEs decreases from La^{3+} (z=57) to Lu^{3+} (z=71), resulting in closer packing of the ion groups and subsequently, shortening of the chemical bonds between metal and oxygen (Begun et al. 1981). This shortening causes a shift in the spectral features toward the shorter wavelengths. Spectral shifts can also occur as a result of different viewing geometries of the sample (e.g. Salisbury et al., 1991; Zhang and Salje, 2001), different data acquisition settings (e.g. the sampling interval), spectral resolutions and signal-to-noise ratios of the different spectrometers. It should be noted that in general, the wavelengths of the spectral features reported in this study are in general in good agreement with those shown in Chukanov (2014). Since spectral shifting can be triggered by many different factors, and these shifts can be relative rather than absolute, information that could potentially be obtained on the presence of specific REEs must be carefully considered.

Third, the hyperspectral imaging spectrometers currently available in the long-wave infrared wavelength only cover the wavelength range nominally between 7.7-12 µm (ITRES TASI, Specim Aisa OWL, Telops Hyper-Cam). The operative range of these instruments is in the range of minimal atmospheric signal attenuation in the broader long-wave infrared range, a phenomenon that increasingly obscures emitted energy beyond the 14 µm threshold wavelength range (Itakura et al., 1974). However, unfortunate for the detection of the REEs by hyperspectral imaging, our results indicate that this wavelength range does not provide direct information on the presence or chemistry of different REEs, despite the study by Sheibley and Fowler (1966) suggesting that the rare earth oxides Dy_2O_3, Er_2O_3, Eu_2O_3, Gd_2O_3, Ho_2O_3, La_2O_3, Pr_6O_{11}, Sm_2O_3 and Yb_2O_3, potentially analogous to REE-bearing minerals, have a subtle spectral feature near 12 µm. This feature could not be observed in the mineral spectra of this study, potentially due to the masking of strong spectral features associated with different mineral groups, discussed above.

The rare earth oxides show spectral features near 14-15 µm and at longer wavelengths (Sheibley and Fowler, 1966). This is the region of the external vibrations that can involve the movements of Ce^{3+} ions (Ruschel et al., 2012), also discussed above in the context of the spectral features predicted in the Dieke diagram (Dieke, 1968). This is the wavelength range of the v_2 and v_4 antisymmetric bending modes of the phosphate (Ross, 1974) and silicate (Farmer, 1974; Salisbury et al., 1991) ions, and those of the v_4 bending modes of the carbonate ions (Adler and Kerr, 1963; White, 1974). Furthermore, studies by Hezel and Ross (1966) and Silva et al. (2006), conducted on synthetic orthophosphate crystals, suggest that REE-O vibrations occur in the 22-40 µm wavelength region. Although these long wavelength regions are currently not available using commercial imaging spectrometers, their potential could be investigated for the remote detection of different REEs. However, this wavelength range extends beyond the 8-14 µm atmospheric window (Itakura et al., 1974) which may preclude any form of remote sensing. Nevertheless, even if

limited to controlled laboratory conditions, such an approach could be beneficiary for many mineral exploration and exploitation applications (e.g. sorting).

7. Conclusions

We have investigated the spectral features of a set of economically important, REE-bearing samples in the LWIR wavelength region. Our results suggest that the REEs do not induce resolvable diagnostic spectral features in the 8-12 μm wavelength range, a range that is dominated by the fundamental stretching modes of the different mineral groups. Longer wavelengths (14-40 μm) have the potential to be used for the direct detection of the REEs, but the commercially available spectrometers need to overcome the challenge of a strong atmospheric attenuation beyond the current limit of 12 μm for these wavelengths to be widely available for mineralogical applications in proximal sensing.

References

Adler, H.H., Kerr, P.F., 1963. Infrared spectra, symmetry and structure relations of some carbonate minerals. Am. Min. 48, 839-853.

Begun, G.M., Beall, G.W., Boatner, L.A., Gregor, W.J., 1981. Raman spectra of the rare earth ortophosphates. J. Raman Spectrosc. 11, 273-278. https://doi.org/10.1002/jrs.1250110411.

Binnemans, K., Jones, P.T., 2015. Rare earths and the balance problem. J. Sustain. Metall. 1, 29-38. https://doi.org/10.1007/s40831-014-0005-1.

Boesche, N.K., Rogass, C., Lubitz, C., Brell, M., Herrmann, S., Mielke, C., Tonn, S., Appelt, O., Altenberger, U., Kaufmann, H., 2015. Hyperspectral REE (rare earth element) mapping of outcrops – applications for neodymium detection. Rem. Sens. 7, 5160-5186. Https://doi.org/10.3390/rs70505160.

Christensen, P.R., Bandfield, J.L., Hamilton, V.E., Howard, D.A., Lane, M.D., Piatek, J.L., Ruff, S.W., Stefanov, W.L., 2000. A thermal emission spectral library of rock-forming minerals. J. Geophys. Res. 105, 9735-9739. https://doi.org/10.1029/1998JE000624.

Chukanov, N.V., 2014. Infrared spectra of mineral species. Extended library. Volume I, first ed. Springer Geochemistry / Mineralogy, Springer Dordrecht.

Dieke, G.H., (1968). Spectra and energy levels of rare earth ions in crystals. John Wiley and Sons, New York.

388 Duke, E.F., 1994. Near infrared spectra of muscovite, Tschermak substitution, and
389 metamorphic reaction progress: Implications for remote sensing. Geol. 22, 621-624.
390 https://doi.org/10.1130/0091-7613(1994)022<0621:NISOMT>2.3.CO;2.
391
392 European Commission, 2017. Communication from the commission to the European
393 Parliament, the Council, the European Economic and Social Committee and the Committee
394 of the Regions on the 2017 list of Critical Raw Materials for the EU. https://eur-
395 lex.europa.eu/legal-content/EN/TXT/?uri=COM:2017:490:FIN (accessed 21 Oct 2018).
396
397 Farmer, V.C., 1974. Orthosilicates, pyrosilicates, and other finite-chain silicates. Chapter 13,
398 in: Farmer, V.C. (Ed.), The infrared spectra of minerals. Mineralogical Society, London, pp.
399 285-303.
400
401 Feng, J., Rogge, D., Rivard, B., 2018. Comparison of lithological mapping results from
402 airborne hyperspectral VNIR-SWIR, LWIR and combined data. Int. J. Appl. Earth Obs.
403 Geoinf. 64, 340-353. https://doi.org/10.1016/j.jag.2017.03.003.
404
405 Frost, R.L., Dickfos, M.J., 2007. Raman spectroscopy of halogen-containing carbonates. J.
406 Raman Spectrosc. 38, 1516-1522. https://doi.org/10.1002/jrs.1806.
407
408 Frost, R.L., López, A., Scholz, R., Yunfei, X., Belotti, F.M., 2013. Infrared and Raman
409 spectroscopic characterization of the carbonate mineral huanghoite – and in comparison
410 with selected rare earth carbonates. J. Mol. Struct. 1051, 221-225.
411 https://doi.org/10.1016/j.molstruc.2013.07.051.

412 Frost, R.L., Scholz, R., Belotti, F.M., López, A., Theiss, F.L., 2015. A vibrational
413 spectroscopic study of the phosphate mineral vantasselite $Al_4(PO_4)_3(OH)_3 \cdot 9H_2O$.
414 Spectrochim. Acta, Part A: Molec. and Biomolec. Spectroscopy 147, 185-192.
415 https://doi.org/10.1016/j.saa.2015.03.090.
416
417 Gunasekaran, S., Anbalagan, G., Pandi, S., 2006. Raman and infrared spectra of
418 carbonates of calcite structure. J. Raman Spectrosc. 37, 892-899.
419 https://doi.org/10.1002/jrs.1518.
420
421 Harris, L., Warren, M., Grant, M., Llewellyn, G.M., 2017. Spectral characterization of the
422 AisaOWL. IEEE Trans. Geosci. Remote Sens. 55(5), 2751-2756.
423 https://doi.org/10.1109/TGRS.2017.2653241.
424
425 Heuser, J., Bukaemskiy, A.A., Neumeier, S., Neumann, A., Bosbach, D., 2014. Raman and
426 infrared spectroscopy of monazite-type ceramics used for nuclear waste conditioning. Prog.
427 Nucl. Energy 72, 149-155. https://doi.org/10.1016/j.pnucene.2013.09.003.
428
429 Hezel, A., Ross, S.D., 1966. Forbidden transitions in the infra-red spectra of tetrahedral
430 anions – III. Spectra-structure correlations in perchlorates, sulphates and phosphates of the
431 formula MXO_4. Spectrochim. Acta 22, 1949-1961. https://doi.org/10.1016/0371-
432 1951(66)80183-2.
433
434 Hunt, G.R., Salisbury, J.W., Lenhoff, C.J., 1972. Visible and near-infrared spectra of
435 minerals and rocks: V. Halides, phosphates, arsenates, vanadates and borates. Mod. Geol.
436 3, 121-132.
437
438 Itakura, Y., Tsutsumi, S., Takagi, T., 1974. Statistical properties of the background noise for
439 the atmospheric windows in the intermediate infrared region. Infrared Phys. 14, 17-29.
440 https://doi.org/10.1016/0020-0891(74)90005-0.

441

442 Keshava, N., Mustard, J.F., 2002. Spectral unmixing. IEEE Signal Process. Mag. 19(1), 44-
443 57. https://doi.org/10.1109/79.974727.

444

445 Kijkowska, R., Cholewka, E., Duszak, B., 2003. X-ray diffraction and Ir-absorption
446 characteristics of lanthanide orthophosphates obtained by crystallisation from phosphoric
447 acid solution. J. Mat. Sci. 38, 223-228. https://doi.org/10.1023/A:1021188810349.

448

449 Kokaly, R.F., Clark, R.N., Swayze, G.A., Livo, K.E., Hoefen, T.M., Pearson, N.C., Wise,
450 R.A., Benzel, W.M., Lowers, H.A., Driscoll, R.L., Klein, A.J., 2017. USGS Spectral Library
451 Version 7: U.S. Geological Survey Data Series 1035. https://doi.org/10.3133/ds1035.

452

453 Kravitz, L.C., Kingsley, J.D., Elkin, E.L., 1968. Raman and infrared studies of coupled PO_4^{-3}
454 vibrations. J. Chem. Phys. 49, 4600-4610. https://doi.org/10.1063/1.1669918.

455

456 Lafuente, B, Downs R.T., Yang, H., Stone, N. 2015. The power of databases: the RRUFF
457 project, in: Armbruster, T., Danisi, R.M. (Eds.), Highlights in Mineralogical Crystallography,
458 Walter De Gruyter, Berlin.

459

460 Lippincott, E.R., Van Valkenburg, A., Weir, C.E., Bunting, E.N., 1958. Infrared studies on
461 polymorphs of silicon dioxide and germanium dioxide. J. Res. Natl. Bur. Stand. 61. Research
462 Paper 2885, 61-70. https://doi.org/10.6028/jres.061.009.

463

464 Neave, D.A., Black, M., Riley, T.R., Gibson, S.A., Ferrier, G., Wall, F., Broom-Fendley, S.,
465 2016. On the feasibility of imaging carbonatite-hosted rare earth element deposits using
466 remote sensing. Econ. Geol. 111, 641-665. https://doi.org/10.2113/econgeo.111.3.641.

467

468 Rastsvetaeva, R.K., Chukanov, N.V., Viktorova, K.A., Aksenov, S.M., 2018. New Data on
469 Isomorphism in Eudialyte-Group Minerals. I. Crystal Structure of Titanium-Rich Eudialyte
470 from the Kovdor Alkaline Massif. Crystallogr. Rep. 63, 563-569. Original (in Russian):
471 Rastsvetaeva, R.K., Chukanov, N.V., Viktorova, K.A. and Aksenov, S.M., 2018. Krist. 63(4),
472 559–566.

473

474 Ross, S.D., 1974. Phosphates and other oxy-anions of group V. Chapter 17, in: Farmer,
475 V.C. (Ed.), The infrared spectra of minerals. Mineralogical Society, London, pp. 383-419.

476

477 Rowan, L.C., Kingston, M.J., Crowley, J.K., 1986. Spectral reflectance of carbonatites and
478 related alkalic igneous rocks: Selected samples from four North American localities. Econ.
479 Geol. 81, 857-871. https://doi.org/10.2113/gsecongeo.81.4.857.

480

481 Ruschel, K., Nasdala, L., Kronz, A., Hanchar, J.M., Többens, D.M., Škoda, R., Finger, F.,
482 Möller, A., 2012. A Raman spectroscopic study on the structural disorder of monazite-(Ce).
483 Mineral. Petrol. 105, 41-55. https://doi.org/10.1007/s00710-012-0197-7.

484

485 Salisbury, J.W., Walter, L.S., Vergo, N., 1987. Mid-infrared (2.1-25 μm) spectra of minerals.
486 U.S. Geological Survey Open-file report 87-263.
487 https://doi.org/10.3133/ofr87263 (accessed 21 Oct 2018).

488

489 Salisbury, J.W., Walter, L.S., Vergo, N., D'Aria, D.M. 1991. Infrared (2.1-25 μm) spectra of
490 minerals. John Hopkins University Press, Baltimore.

491

492 Sheibley, D.W., Fowler, M.H., 1966. Infrared spectra of various metal oxides in the region of
493 2 to 26 microns. NASA Technical Note TN D-3750.
494 https://ntrs.nasa.gov/archive/nasa/casi.ntrs.nasa.gov/19670003469.pdf (accessed 21 Oct
495 2018).

496
497 Silva, E.N., Ayala, A.P., Guedes,I., Paschoal, C.W.A., Moreira, R.L., Loong, C.-K., Boatner,
498 L.A., 2006. Vibrational spectra of monazite-type rare earth orthophosphates. Opt. Mat. 29,
499 224-230. https://doi.org/10.1016/j.optmat.2005.09.001.
500
501 Turner, D.J., 2015. Reflectance spectroscopy and imaging spectroscopy of rare earth
502 element-bearing mineral and rock samples. PhD Thesis of the University of British
503 Columbia. https://doi.org/10.14288/1.0167182.
504
505 Turner, D.J., Rivard, B., Groat, L.A., 2014. Visible and short-wave infrared reflectance
506 spectroscopy of REE fluorocarbonates. Am. Min. 99, 1335-1346.
507 https://doi.org/10.2138/am.2014.4674.
508
509 Turner, D.J., Rivard, B., Groat, L.A., 2016. Visible and short-wave infrared reflectance
510 spectroscopy of REE phosphate minerals. Am. Min. 101, 2264-2278.
511 https://doi.org/10.2138/am-2016-5692.
512
513 Turner, D.J., Rivard, B., Groat, L.A., 2018. Visible and short-wave infrared reflectance
514 spectroscopy of selected REE-bearing silicate minerals. Am. Min. 103, 927-943.
515 https://doi.org/10.2138/am-2018-6195.
516
517 U.S. Department of Energy, 2011. Critical Materials Strategy.
518 https://www.energy.gov/sites/prod/files/DOE_CMS2011_FINAL_Full.pdf (accessed 21 Oct
519 2018).
520
521 U.S. Geological Survey, 2018. Mineral commodity summaries 2018: U.S. Geological Survey,
522 200 p., https://doi.org/10.3133/70194932 (accessed 21 Oct 2018).
523
524 White, W.B., 1974. The carbonate minerals. Chapter 12, in Farmer, V.C. (Ed.), The infrared
525 spectra of minerals. Mineralogical Society, London, pp. 227-284.

526 Zhang, M., Salje, E.K.H., Ewing, R.C., Farnan, I., Ríos, S., Schlüter, J., Leggo, P., 2000.
527 Alpha-decay damage and recrystallization in zircon: evidence for an intermediate state from
528 infrared spectroscopy. J. Phys.: Cond. Matter 12, 5189-5199. https://doi.org/10.1088/0953-
529 8984/12/24/310.

530 Zhang, M., Salje, E.K.H., 2001. Infrared spectroscopic analysis of zircon: Radiation damage
531 and the metamict state. J. Phys.: Cond. Matter 13, 3057-3071. https://doi.org/10.1088/0953-
532 8984/13/13/317.
533
534

535 **Figures**

536

537 **Fig. 1.** Bastnasite and parisite spectra (samples 1 and 2, respectively). The arrows point to
538 the spectral features labeled as *f1-f2*. Photographs of samples shown at right.

539

540 **Fig. 2. a.** Monazite spectrum (sample 3). **b.** Xenotime spectrum (sample 4). **c.** Xenotime
541 spectra of the samples 5 and 6. The arrows point to the spectral features labeled as *f3-f5*.
542 Photographs of samples shown at right.

543

544 **Fig. 3.** Eudialyte spectra of the samples 7-9. The arrows point to the spectral features
545 labeled as *f6-f8*. Photographs of samples shown at right.

546

547   **Fig. 4. a.** Mosandrite spectrum (sample 10). **b.** Zircon spectra of the samples 11 and 12.
548   The arrows point to the spectral features labeled as *f6-f8*. Photographs of samples shown at
549   right.
550

551   **Tables**

552

553   **Table 1.** Sample information, including mineral identity, ideal formulae, number of pixels
554   averaged, dimensions, mineral group and locality.

555

556   **Table 2.** Electron probe micro analysis (EPMA) results of the samples and number (#) of
557   averaged spot analyses. Further details available in Turner (2015).

558

559   **Table 3.** The spectral features *f1-f8* of the samples (1-12) shown in figures 1-4 and
560   discussed in the text. The wavelength/wavenumber refers to the highest reflectance value
561   (reflectance maximum) of each spectral feature.
562
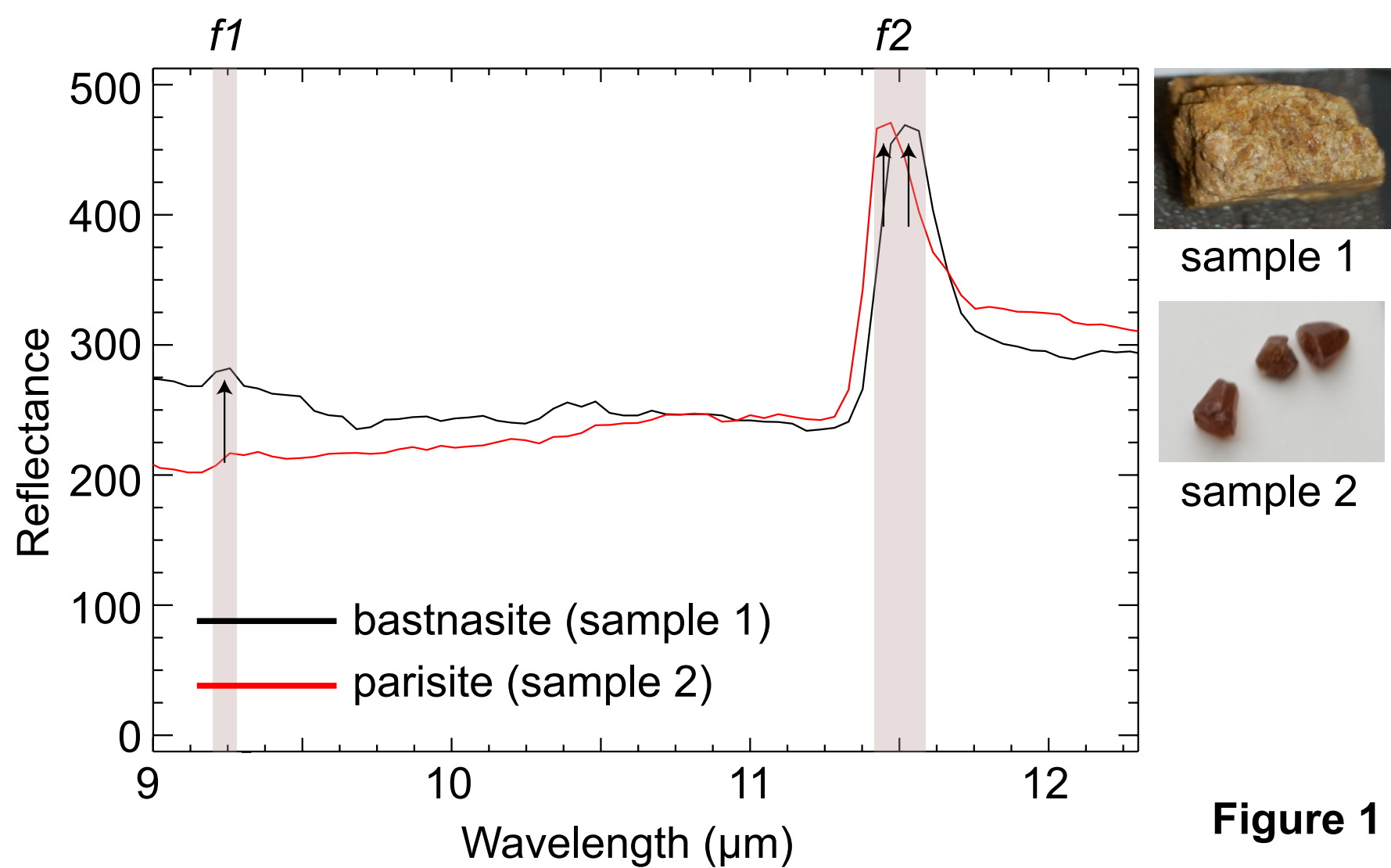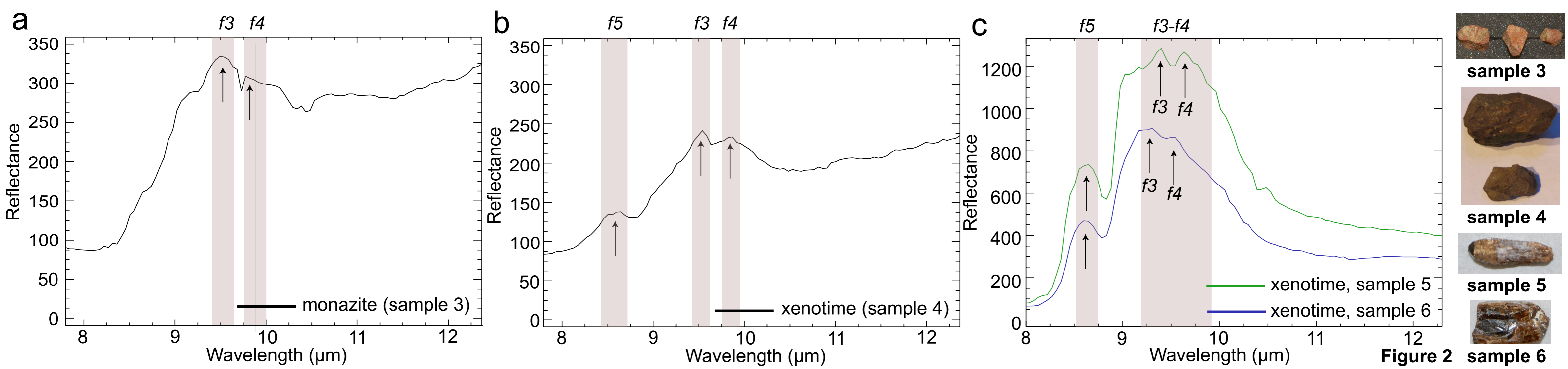
Figure 1

Figure 2

Figure 3

Figure 4

Table 1

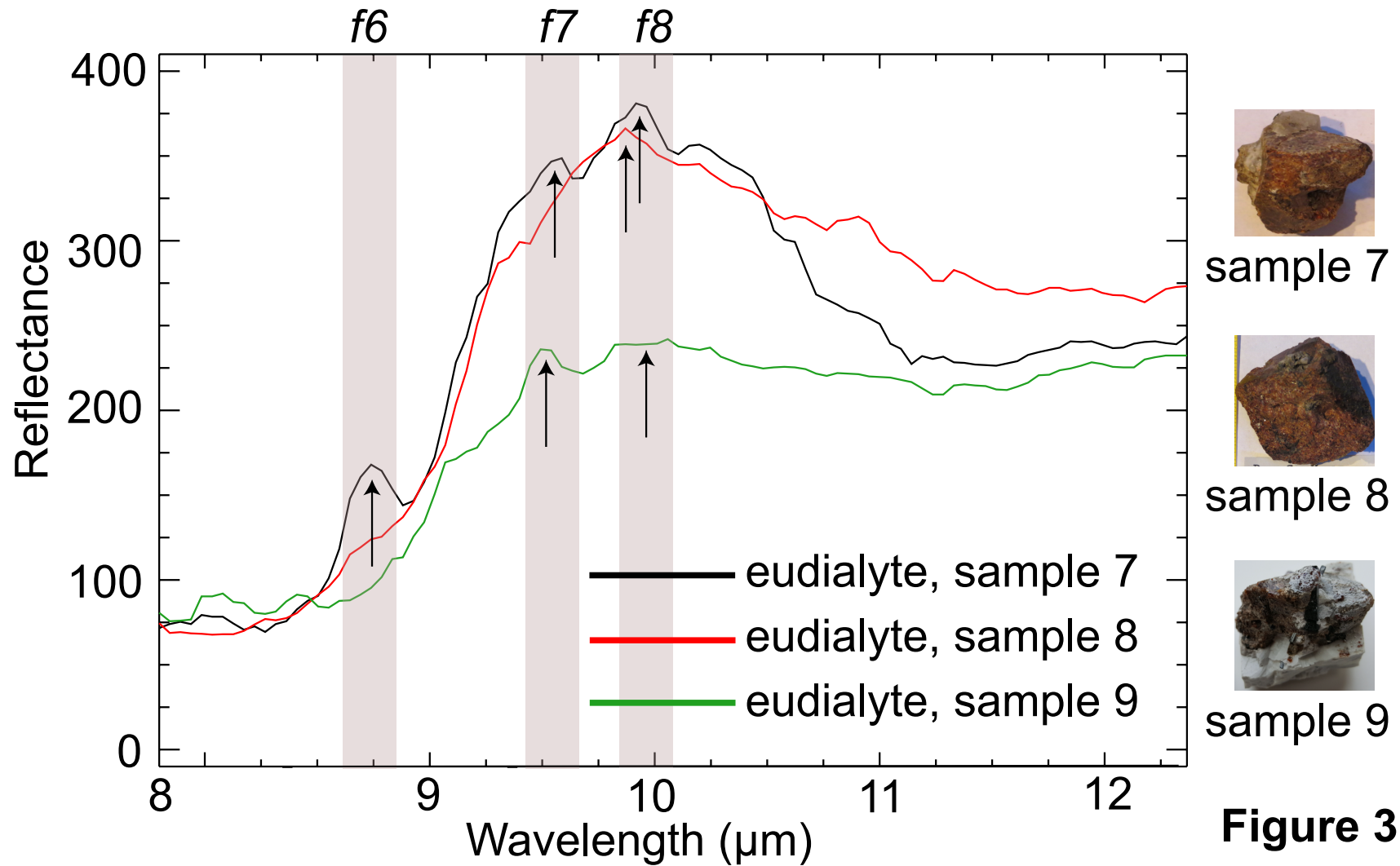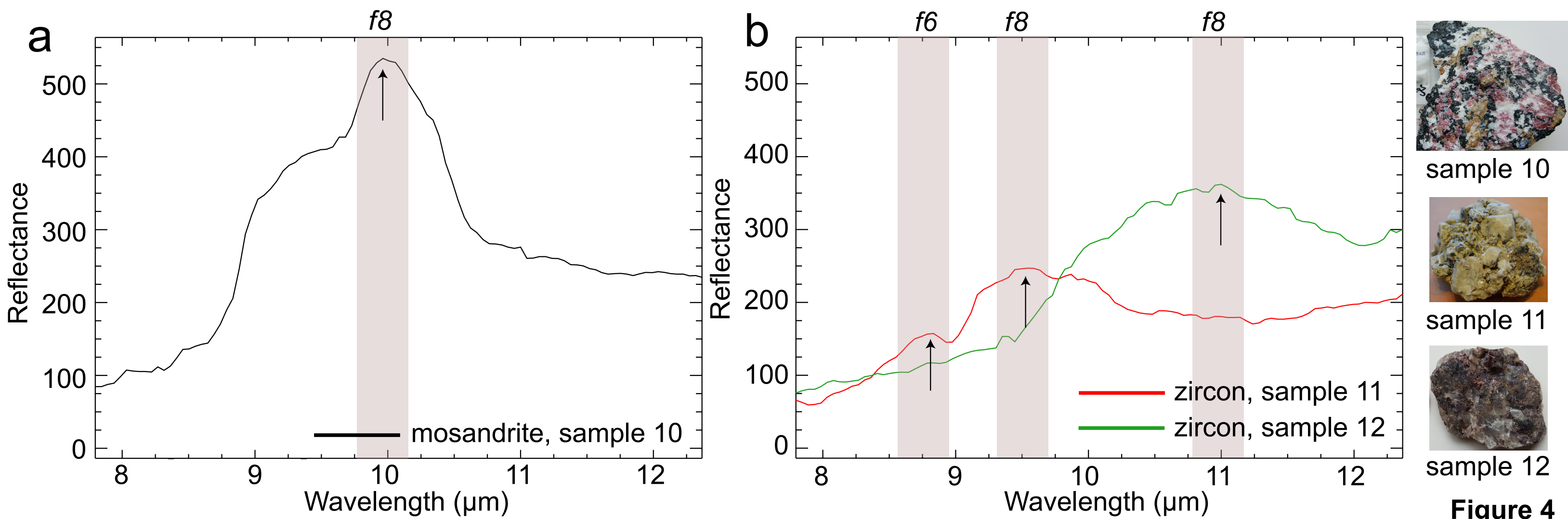| Sample id	Mineral	Ideal formulae	# of pixels	Sample dimensions (mm)	Mineral group	Locality
1	bastnäsite	$(Ce,La)(CO_3)F$	4	30 x 30 x 20	carbonate	Diao Loa Shan, Sichuan, China
2	parisite	$Ca(Ce,La)_2(CO_3)_3F_2$	4	5 x 5 x 5	carbonate	Muzo, Columbia
3	monazite	$(Ce,La, Nd, Th)PO_4$	3	10 x 10 x 10	phosphate	Elk Mountain, Nebraska, USA
4	xenotime	YPO_4	3	17.5 x 25 x 20	phosphate	Gunter Quarry, Ontario, Canada
5	xenotime	YPO_4	3	22.5 x 7.5 x 7.5	phosphate	Novo Horizonte (sample "C"), Brazil
6	xenotime	YPO_4	4	25 x 14 x 10	phosphate	Novo Horizonte (sample "J"), Brazil
7	eudialyte	$Na_4(Ca, Ce)_2(Fe^{2+}, Mn^{2+})ZrSi_8O_{22}(OH, Cl)_2(?)$	3	15 x 15 x 20	silicate	Mont St. Hilaire, Rouville, Quebec, Canada (sample 72-24)
8	eudialyte	$Na_4(Ca, Ce)_2(Fe^{2+}, Mn^{2+})ZrSi_8O_{22}(OH, Cl)_2(?)$	4	25 x 25 x 20	silicate	Mont St. Hilaire, Rouville, Quebec, Canada (sample MSH CMNOC 37104)
9	eudialyte	$Na_4(Ca, Ce)_2(Fe^{2+}, Mn^{2+})ZrSi_8O_{22}(OH, Cl)_2(?)$	3	35 x 20 x 20	silicate	Mont St. Hilaire, Rouville, Quebec, Canada (sample 88-79)
10	mosandrite	$(Ca_3REE)[(H_2O)_2Ca_{0.5}\square_{0.5}]Ti(Si_2O_7)_2(OH)_2(H2O)_2$	3	Crystal clusters up to 25 x 10	silicate	Kipawa, Ontario, Canada (sample F92-23)
11	zircon	$ZrSiO_4$	4	Crystal clusters up to 7.5 x 7.5	silicate	Mount Malosa, Malawi
12	zircon	$ZrSiO_4$	4	Crystals up to 8 x 8	silicate	St Peter's Dome, Colorado, USA

Table 2

Sample id	1	2	3	4	5	6	7	8	9	10	11	12
# Analyses	*10*	*6*	*5*	*5*	*5*	*5*	*5*	*5*	*5*	*5*	*5*	*5*
Nb_2O_5 (wt.%)	0.01	0.00	0.00	0.08	0.07	0.08	2.48	1.96	2.24	1.61	1.53	0.19
P_2O_5	0.00	0.00	22.62	34.16	29.12	30.83	0.01	0.01	0.01	0.02	0.24	0.10
SiO_2	0.05	0.06	1.90	0.53	0.20	0.23	51.31	53.21	49.98	29.76	30.65	31.70
TiO_2	0.00	0.00	0.00	0.00	0.00	0.01	0.32	0.29	0.10	8.29	0.03	0.00
ZrO_2	0.00	0.00	0.02	0.17	0.13	0.11	11.19	11.73	12.27	0.44	58.01	63.70
UO_2	0.53	0.39	0.32	0.58	0.07	0.01	0.03	0.07	0.00	0	0.00	0.00
ThO_2	0.14	0.83	12.15	0.53	0.07	0.33	0.11	0.09	0.14	0.1	0.29	0.03
Al_2O_3	0.00	0.00	0.00	0.01	0.00	0.00	0.06	0.06	0.13	0.06	0.00	0.00
La_2O_3	27.77	14.03	10.60	0.00	0.00	0.00	1.01	1.05	1.48	1.47	0.02	0.00
Ce_2O_3	31.13	26.11	22.98	0.00	0.00	0.02	1.93	1.88	2.93	4.02	0.24	0.00
Pr_2O_3	2.50	2.90	3.03	0.01	0.00	0.00	0.17	0.15	0.30	0.54	0.05	0.00
Nd_2O_3	7.25	11.90	11.86	0.15	0.05	0.08	0.59	0.52	0.92	2.51	0.48	0.00
Sm_2O_3	0.47	1.85	4.94	0.34	1.05	0.70	0.08	0.07	0.16	0.74	0.42	0.00
Eu_2O_3	0.00	0.03	0.12	0.00	0.35	0.12	0	0.00	0.00	0.09	0.04	0.00
Gd_2O_3	0.20	1.06	2.83	1.46	5.71	3.88	0.05	0.05	0.12	0.82	0.37	0.00
Tb_2O_3	0.00	0.00	0.48	0.33	1.48	1.02	0	0.00	0.00	0.14	0.00	0.00
Dy_2O_3	0.00	0.00	1.64	3.58	9.75	7.73	0.02	0.00	0.04	1.05	0.29	0.01
Ho_2O_3	0.00	0.00	0.00	1.02	1.72	1.67	0.01	0.00	0.01	0.21	0.05	0.01
Er_2O_3	0.00	0.00	0.08	3.88	4.94	5.26	0.01	0.01	0.02	0.57	0.16	0.01
Tm_2O_3	0.00	0.00	0.00	0.61	0.51	0.54	0	0.00	0.00	0.05	0.02	0.00
Yb_2O_3	0.00	0.00	0.00	5.15	2.14	2.51	0.01	0.00	0.01	0.32	0.30	0.04
Lu_2O_3	0.00	0.00	0.00	0.82	0.11	0.23	0.00	0.00	0.00	0	0.00	0.00
Y_2O_3	0.01	0.74	0.45	45.72	41.82	44.51	0.35	0.34	0.62	5.96	2.39	0.03
SrO	0.01	0.00	0.00	0.00	0.00	0.00	0.32	0.26	0.29	0.09	0.12	0.13
MgO	0.00	0.00	0.00	0.00	0.00	0.00	0.02	0.02	0.03	0.03	0.00	0.01
FeO	0.00	0.00	0.00	0.00	0.02	0.00	2.62	2.47	2.93	0.05	0.03	0.00
BaO	0.00	0.00	0.00	0.01	0.00	0.00	0.02	0.06	0.01	0.00	0.00	0.00
CaO	0.11	10.48	0.64	0.01	0.00	0.00	5.53	5.75	3.78	26.68	0.00	0.00
MnO	0.00	0.00	0.00	0.00	0.00	0.00	9.14	8.60	7.90	0.05	0.05	0.02
Na_2O	0.03	0.01	0.02	0.00	0.01	0.00	5.73	4.46	6.21	6.39	0.01	0.00
Cl	0.01	0.02	0.02	0.02	0.00	0.00	0.39	0.45	0.53	0.02	0.00	0.01
F	5.22	4.48	0.36	0.51	0.30	0.33	0.18	0.08	0.19	4.63	0.04	0.03
O=CL	0.00	0.00	0.00	0.00	0.00	0.00	-0.09	-0.10	-0.12	0.00	0.00	0.00
O=F	-2.20	-1.89	-0.15	-0.21	-0.13	-0.14	-0.08	-0.03	-0.08	-1.95	-0.02	-0.01
TOTAL	93.50	98.37	96.90	99.46	99.49	100.06	95.15	95.09	94.76	99.30	95.82	96.04
REE_2O_3	69.35	58.61	59.01	63.07	69.63	68.27	4.23	4.07	6.61	18.49	4.83	0.10

Table 3

Fig.	Sample id	Feature	Wavelength (µm)	Wavenumber (cm-1)
1	1	f1	9.257	1080.26
1	1	f2	11.518	868.21
1	2	f2	11.471	871.76
2A	3	f3	9.493	1053.41
2A	3	f4	9.776	1022.91
2B	4	f3	9.540	1048.22
2B	4	f4	9.870	1013.17
2B	4	f5	8.645	1156.74
2C	5	f3	9.399	1063.94
2C	5	f4	9.634	1037.99
2C	5	f5	8.645	1156.74
2C	6	f3	9.304	1074.81
2C	6	f4	9.540	1048.22
2C	6	f5	8.645	1156.74
3	7	f6	8.739	1144.30
3	7	f7	9.587	1043.08
3	7	f8	9.917	1008.37
3	8	f8	9.870	1013.17
3	9	f7	9.493	1053.41
3	9	f8	9.917	1008.37
4A	10	f8	9.964	1003.61
4B	11	f6	8.833	1132.12
4B	11	f8	9.540	1048.22
4B	12	f8	11.000	909.09